ARTICLES
PUBLISHED ONLINE: 14 APRIL 2013 | DOI: 10.1038/NPHOTON.2013.57
nature photonics

# Damping pathways of mid-infrared plasmons in graphene nanostructures

Hugen Yan[1†]*, Tony Low[1†], Wenjuan Zhu[1], Yanqing Wu[1], Marcus Freitag[1], Xuesong Li[1], Francisco Guinea[2], Phaedon Avouris[1]* and Fengnian Xia[1]*

**Plasmon is the quantum of the collective oscillation of electrons. How plasmon loses its energy (or damping) plays a pivotal role in plasmonic science and technology. Graphene plasmon is of particular interest, partly because of its potentially low damping rate. However, to date, damping pathways have not been clearly unravelled experimentally. Here, we demonstrate mid-infrared (4–15 μm) plasmons in graphene nanostructures with dimensions as small as 50 nm (with a mode area of $\sim 1 \times 10^{-3}$ μm$^2$). We also reveal damping channels via graphene intrinsic optical phonons and scattering from the edges. Plasmon lifetimes of 20 fs or less are observed when damping via the emission of graphene optical phonons is allowed. Furthermore, surface polar phonons in the $SiO_2$ substrate under graphene nanostructures lead to a significantly modified plasmon dispersion and damping, in contrast to the case of a nonpolar diamond-like-carbon substrate. Our study paves the way for applications of graphene in plasmonic waveguides, modulators and detectors from sub-terahertz to mid-infrared regimes.**

Plasmonic nanostructures allow the confinement of electromagnetic energy beyond the diffraction limit, enabling applications ranging from metamaterials, quantum optics and photovoltaics to photodetectors and biological sensing[1]. Graphene plasmons in particular have attracted great interest, because of their unique tunability[2–8], presumably long plasmon lifetime[2,9] and high degree of electromagnetic confinement[6,7]. The electromagnetic response of patterned graphene microstructures in the terahertz frequency regime was studied recently[4,8,9] and was found to be dominated by the plasmon excitations of Dirac fermions[4,8]. Here, we demonstrate that the dispersive nature of the two-dimensional plasmon enables engineering of graphene plasmon resonances into the mid-infrared regime by patterning graphene into nanostructures with dimensions as small as 50 nm. In contrast to their microstructure counterparts, in which plasmon resonances lie in the terahertz frequency range, the mid-infrared plasmonic response has been found to be affected strongly by interactions with substrate phonons and intrinsic graphene optical phonons. These interactions lead to the renormalization of the plasmon dispersion and govern the lifetimes and propagation distances of plasmons. Moreover, an edge-related effect on mid-infrared plasmonic responses is explicitly identified, which not only complements previous transport studies on similar graphene nanostructures[10–12], but also the research field concerning localized plasmons in metal nanostructures[13,14].

## Experiments and methodology

Graphene nanostructures such as nanoribbon, antidot and nanodisk arrays were defined using electron-beam lithography on graphene grown by chemical vapour deposition (CVD)[15]. Different supporting substrates, such as $SiO_2$ and diamond-like-carbon (DLC)[16], were used on top of highly resistive silicon wafers. The mid-infrared transmission measurement set-up for these structures (see Fig. 1a) consisted of an infrared microscope coupled to a Fourier-transform infrared spectrometer (FTIR), used in conjunction with a broadband polarizer. Details of the fabrication and measurement procedures are given in the Methods.

The qualitative behaviour of the plasmonic response in graphene nanoribbons and nanodisks is similar, except for a distinct polarization dependence in the former[4,8]. Here, we focus on graphene nanoribbons (see Fig. 1b for a typical scanning electron microscopy (SEM) image). The electromagnetic responses of these graphene nanoribbon arrays are characterized by the extinction spectra $1 - T_{per}/T_0$ and $1 - T_{par}/T_0$, where $T_{per}$ and $T_{par}$ are the transmission of the light through the ribbon array with the electric field perpendicular or parallel to the ribbon, and $T_0$ is the transmission through the substrate without graphene. Figure 1c presents the extinction spectra of a ribbon array on a $SiO_2$ substrate, with ribbon widths of ~240 nm. The two curves show results for incident light with polarization perpendicular (red) and parallel (grey) to the ribbons, respectively. The inset depicts the dipole oscillation in a graphene nanoribbon.

As a result of excitation of localized plasmons, the extinction spectrum with perpendicular polarization shows prominent resonance peaks[4,8]. The multiple resonance peaks observed here are in sharp contrast to the results for far-infrared spectra of graphene microstructures, which usually display a single strong resonance[4,8]. Because of a lack of plasmon excitation, the spectrum with parallel polarization has no resonance peaks, except for small features between 1,000 cm$^{-1}$ and 1,200 cm$^{-1}$. These features are related to the rapidly varying dynamic dielectric function of the $SiO_2$ substrate[17], and are weak (<1% in extinction) in comparison to the prominent plasmon peaks. In this mid-infrared wavelength range, if light polarization is parallel to the highly doped graphene ribbons (as reported in this work), the interaction with light is insignificant due to Pauli blocking of the interband transitions and the weakness of the free-carrier intraband transitions at such high frequencies[18]. As a result, the transmission spectra of the ribbons for parallel polarized light ($T_{par}$) are very close to those of the reference ($T_0$), and in subsequent presentations will serve as a reference for the extinction spectra of perpendicularly polarized light. In other words, the extinction spectrum is defined as $1 - T_{per}/T_{par}$ elsewhere in this Article (see Methods).

[1]IBM Thomas J. Watson Research Center, Yorktown Heights, New York 10598, USA, [2]Instituto de Ciencia de Materiales de Madrid, CSIC, Sor Juana Inés de la Cruz 3, 28049 Madrid, Spain, [†]These authors contributed equally to the work. *e-mail: hyan@us.ibm.com; avouris@us.ibm.com; fxia@us.ibm.com

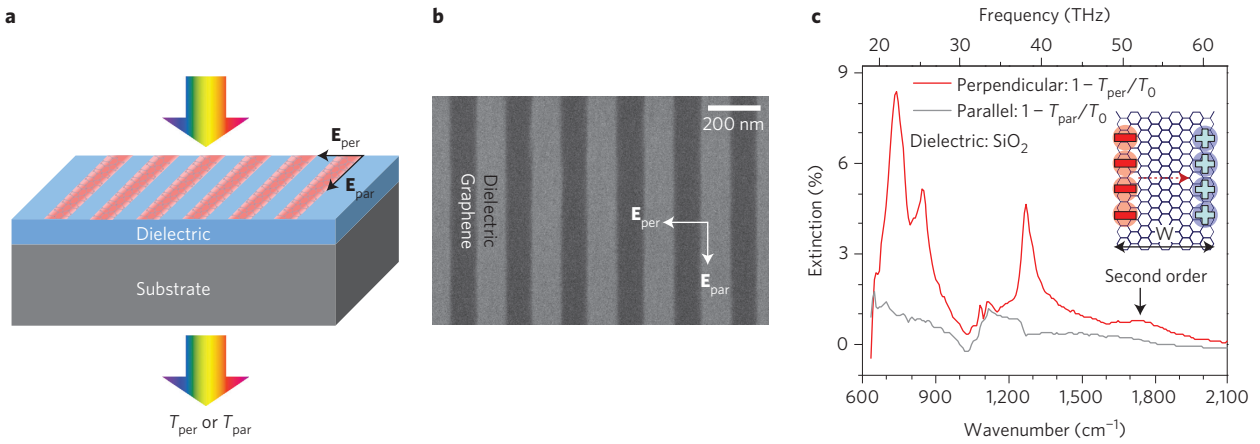


**Figure 1 | Schematics of the experiment. a**, Mid-infrared transmission measurement scheme for graphene nanoribbons. The excitation light is broadband. False colours are used for excitation light (rainbow) and on-resonance light in graphene nanoribbons (red). **b**, SEM image of a typical array of graphene nanoribbons. The width of the ribbon is ~100 nm. **c**, Extinction spectra of a ribbon array on $SiO_2$ with the incident light polarization perpendicular (red) and parallel (grey) to the ribbons. Ribbon width is 240 nm. A weak second-order mode is indicated. Inset: dipole oscillation in a graphene ribbon.

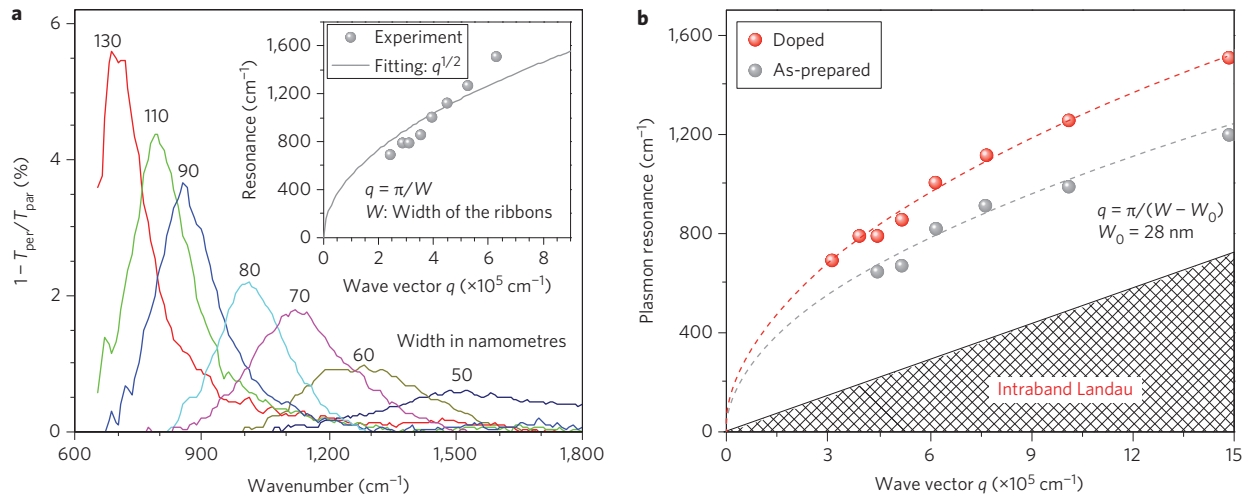


**Figure 2 | Plasmons in graphene nanoribbons on DLC. a**, Extinction spectra ($1 - T_{per}/T_{par}$) of graphene ribbons on DLC with different ribbon widths. The spectra were referenced using transmission of light with parallel polarization ($T_{par}$). Inset: plasmon resonance frequency as a function of wave vector $q = \pi/W$, where $W$ is the width of the nanoribbon. The grey curve is a fit according to $\omega_{pl} \approx \sqrt{q}$. **b**, The same plasmon resonance data (red dots) as in **a**, plotted as a function of wave vector $q = \pi/W_e$, where $W_e = W - W_0$ is the effective ribbon width and $W_0$ is 28 nm . Plasmon resonance data for a lower Fermi level case are also plotted (grey dots). Dashed curves are fits based on $\sqrt{q}$ scaling. The shaded area is the intraband Landau damping region.

The multiple resonance structures observed in the spectra of Fig. 1c are due to interactions of graphene plasmons with substrate phonons. These Fuchs–Kliewer[19] surface optical (SO) phonons are well known in polar semiconductor surfaces and have been studied extensively in conventional two-dimensional electron systems[20,21]. When graphene is placed on a polar substrate such as $SiO_2$ that accommodates these SO phonons, long-range Fröhlich coupling can mediate interactions with the electronic degrees of freedom in graphene[22,23], including the collective plasmon modes[24]. These interactions produce hybridized plasmon–phonon modes in the vicinity of their crossing energies and have recently been observed using techniques such as electron energy loss spectroscopy of epitaxial graphene on SiC substrate[25] and near-field optical nanoscopy of graphene on a $SiO_2$ substrate[5]. It is instructive to first consider a simpler system, that is, graphene on a nonpolar substrate, DLC.

## Plasmons of graphene nanoribbons on DLC substrate

Figure 2a presents extinction spectra for graphene ribbons of various widths $W$ on a DLC substrate. We observe only one prominent plasmon resonance peak for each spectrum, unlike in the spectra for the $SiO_2$ substrate. Here, we expect the plasmon resonance frequency to follow a simple $\sqrt{q}$ dispersion in the long wavelength limit, where $q$ is the plasmon wave vector, as predicted by random phase approximation (RPA) theory for the linear response of two-dimensional electronic systems[26] such as graphene[27,28]. For localized plasmons in graphene ribbons, $q$ is simply given by $\pi/W$ (ref. 29), regardless of the spacing between the ribbons or the period of the array. The inset of Fig. 1c depicts the surface plasmon dipole resonance within the ribbon. The plasmon resonance in a periodical ribbon array is dominated by the dipole resonances within each isolated ribbon, as the ribbon-to-ribbon coupling effects are much weaker[8,30]. The inset of Fig. 2a shows the extracted

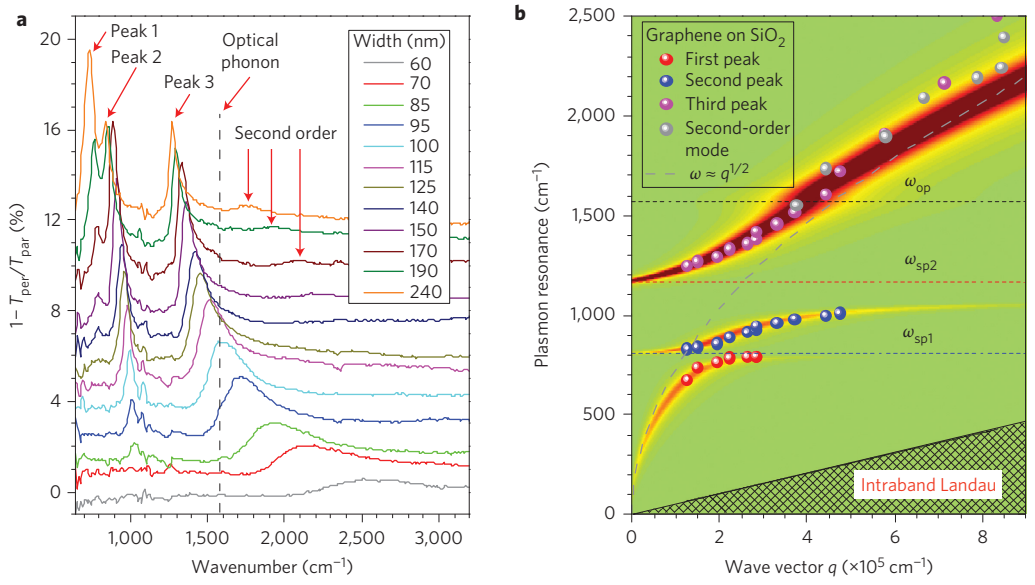


**Figure 3 | Plasmons in graphene nanoribbons on $SiO_2$.** **a**, Extinction spectra ($1 - T_{per}/T_{par}$) of graphene ribbons on $SiO_2$ with different ribbon widths. The spectra are vertically displaced for clarity. The vertical dashed line indicates the graphene optical phonon frequency. **b**, Plasmon frequency as a function of wave vector $q = \pi/W_e$ for peaks 1, 2 and 3 and a second-order dipolar mode peak in **a**. The calculated loss function is plotted as a two-dimensional pseudocolour background. The dashed line represents the plasmon frequency without considering plasmon–phonon hybridization. Two surface polar phonons and the intrinsic optical phonon frequencies are indicated. See Supplementary Section SI for details of modelling.

plasmon frequencies from Fig. 2a as a function of $\pi/W$, where there is clear disagreement with the simple scaling $\omega_{pl} \propto \sqrt{(\pi/W)}$ predicted by theory. This discrepancy is not due to breakdown of the long-wavelength approximation, and correction caused by the quantum confinement effect is also negligible for dimensions larger than 10 nm (ref. 31).

Earlier experiments with graphene nanoribbons have shown that it is often necessary to postulate an electrical width smaller than the physical width in order to explain electrical transport behaviour[10–12]. Indeed, fabrication of graphene ribbons by electron-beam lithography and oxygen plasma etching can impart atomic-scale defects and complicated edge chemistry[32] that render the edges electrically 'inactive'[33]. In a similar fashion, we introduce an effective ribbon width defined as $W_e = W - W_0$. Figure 2b displays the plasmon frequency as a function of $q = \pi/W_e$. The dashed lines are $\sqrt{q}$ fittings, and agree very well with experiments for two different doping levels and $W_0 = 28$ nm. Using this methodology with the same $W_0$, we can also explain the more complicated hybrid plasmon–phonon dispersions in graphene on $SiO_2$, as discussed in the next section.

## Plasmons of graphene nanoribbons on $SiO_2$ substrate

Figure 3a presents extinction spectra for graphene ribbons on a $SiO_2$ substrate with $W$ ranging from 60 to 240 nm, demonstrating three major resonance peaks and a weak higher-order resonance[9] within our measured frequency range of 650–6,000 cm$^{-1}$. These ribbons were prepared under similar conditions as used for the ribbons on the DLC substrate, so they have similar doping levels (see Methods). We can identify four key trends in the spectra. The first is dispersion: all resonance peaks blueshift as $W$ decreases, but at very different rates. In particular, peak 3 disperses upwards in frequency at a much faster rate. The second is spectral weight, which is transferred from peak 1 to peaks 2 and 3 with decreasing $W$, until eventually peak 3 retains all of the spectral weight for $W < 90$ nm. The third trend is linewidth. The linewidth of peak 3 increases with decreasing $W$, while the linewidths of peaks 1 and 2 remain almost constant. In fact, the resonance linewidth for ribbons on DLC discussed in the previous section also exhibits the same trend as that of peak 3 in Fig. 3a. The linewidth is directly related to plasmon damping and will be discussed in the next section. The final trend relates to line shape: peak 3 is very asymmetric, especially in relatively narrow ribbons. As detailed in Supplementary Section SIII, the line shape can be well described by a Fano resonance model[34].

The multiple resonances observed in the spectra are ascribed to plasmon–phonon coupled modes and can be described within a generalized RPA theory[24,35,36]. Directly relevant to our experiments is the loss function $\Im\left[1/\varepsilon_T^{rpa}\right]$, defined as the imaginary part of the inverse dielectric function, which represents the ability of the system to dissipate energy via plasmon excitations. Our calculations include both interactions with the relevant substrate SO phonons of $SiO_2$[17] at $\omega_{sp1} = 806$ cm$^{-1}$ and $\omega_{sp2} = 1{,}168$ cm$^{-1}$ and the graphene intrinsic optical phonon modes[37] at $\omega_{op} = 1{,}580$ cm$^{-1}$. A detailed discussion is provided in Supplementary Section SI. It is worth mentioning that the surface polar phonon itself can also be excited by light, leading to phonon–polariton resonance. This has been demonstrated using infrared nanoscopy on SiC surfaces[38]. Similar to plasmons, this phonon–polariton can also dramatically confine the electromagnetic wave.

Figure 3b presents an intensity plot of the loss function overlaid on the resonance peak frequencies obtained from the spectra in Fig. 3a. We applied the same methodology used in the previous section, that is, defining the wave vector of the localized plasmon to be $q = \pi/(W - W_0)$, with $W_0 = 28$ nm. Excellent agreement with the experimentally observed plasmon–phonon dispersions can be obtained using a Fröhlich coupling strength of $F_{sp1}^2 \approx 0.2$ meV and $F_{sp2}^2 \approx 2$ meV, where the latter takes into account the mode's double degeneracy. The value of the Fröhlich coupling quantifies the hybridization of the plasmon–phonon mode and the anticrossing energy splitting, and is defined as

$$F_{sp}^2 = \frac{\hbar\omega_{sp}}{2\pi}\left(\frac{1}{\varepsilon_{high} + \varepsilon_0} - \frac{1}{\varepsilon_{low} + \varepsilon_0}\right)$$

(Supplementary Section SI), where $\varepsilon_{high}$ and $\varepsilon_{low}$ are the high- and low-frequency dielectric constants of $SiO_2$, respectively. The values

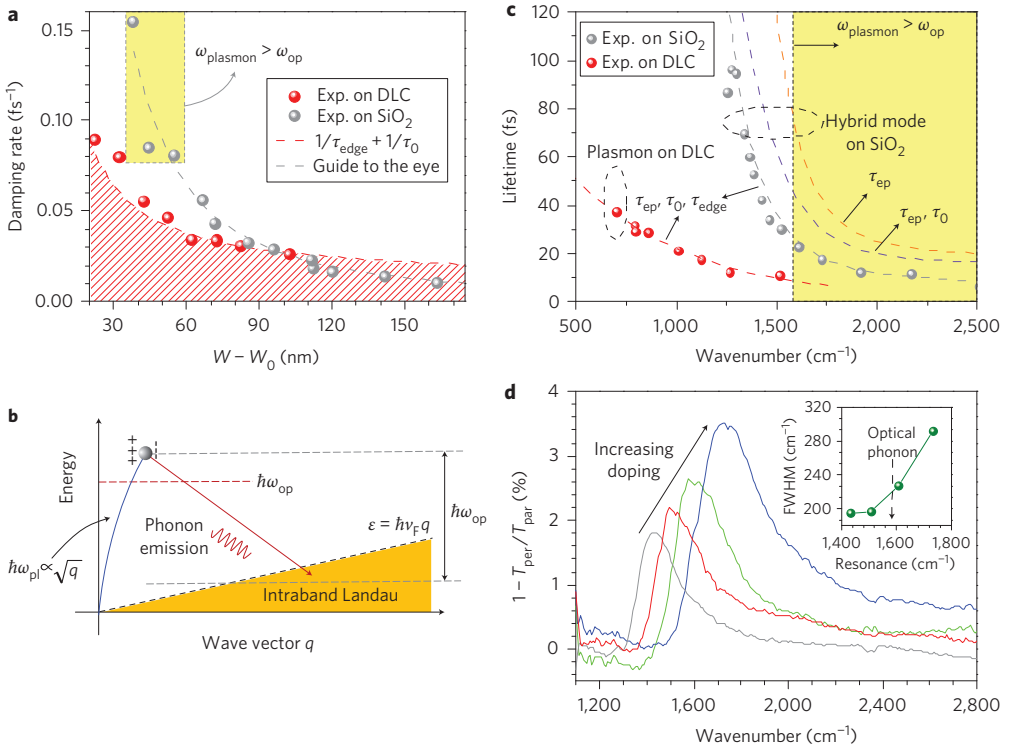


**Figure 4 | Origins of plasmon damping. a**, Damping rates of plasmons of graphene ribbons with similar doping on DLC (red) and $SiO_2$ (grey) as a function of $W_e$. For ribbons on $SiO_2$, peak 3 in Fig. 3a is used. The red dashed curve is a fitted curve (described in the main text) and the grey dashed curve is a guide to the eye using $\Gamma_p \propto (W - W_0)^{-x}$. **b**, Illustration of the plasmon damping process through the emission of an optical phonon, which brings it into the intraband Landau damping regime; electron–hole pairs are created. **c**, Plasmon lifetimes of ribbons on DLC (red dots) and $SiO_2$ (grey dots) as functions of plasmon resonance frequencies. Dashed curves are calculated results, with the orange curve representing plasmon damping via phonon emission only, the blue curve both phonon emission and bulk scattering, and the grey (for $SiO_2$) and red (for DLC) curves for phonon emission, bulk scattering and edge scattering (Supplementary Section SII). **d**, Extinction spectra of a ribbon with $W = 100$ nm on $SiO_2$ at four different doping levels. Inset: extracted full-width at half-maximum (FWHM) as a function of the corresponding plasmon resonance frequency.

extracted from fitting of the hybrid plasmon–phonon dispersions, although of the same order as the quoted values used in the literature[39,40], can serve as a better estimate. In addition, the second-order dipolar mode[9,29], with the wave vector in this case given by $q = 3\pi/(W - W_0)$, also coincides with the dispersion of its fundamental mode. The above agreement further validates the premise that the effective width $W - W_0$ defines the plasmon momentum, and $W_0 = 28$ nm consistently explains both plasmon and hybrid plasmon–phonon dispersions on both DLC and $SiO_2$ substrates. From a comparison of the plasmon dispersion without plasmon–phonon hybridization (dashed curve in Fig. 3b) and the fully RPA calculations, we see that for $q < 0.4 \times 10^5$ cm$^{-1}$, the surface phonon effect causes little deviation from the simple $\sqrt{q}$ dispersion. Hence, the plasmon frequency in microribbons follows the simple scaling relation as previously observed by Ju and colleagues[4]. Furthermore, we note that the loss function can also describe the evolution of the plasmon peak intensity for the three hybrid plasmon–phonon branches, featuring two anticrossings and spectral weight transfer from the low- to high-frequency plasmon branch (peak 3) with increasing $q$ (see also Supplementary Section SI).

## Origins of plasmon damping

Many plasmonic applications can benefit from a long plasmon lifetime[1]. However, depending on the system of interest, plasmon can decay into photons via radiative processes[41] or into electron–hole pairs via inter- or intraband Landau damping[36]. In addition, inelastic scattering with phonons[14,42] and elastic carrier scattering processes[9,14,43] can also contribute to plasmon damping. The former two processes can be ruled out because the contribution from radiative damping in graphene nanostructures is expected to be negligible[8,9] and plasmon excitations in our devices lie outside the Landau damping regime, as indicated in Figs 2b and 3b. However, the latter two processes can be important with large plasmon energies (that is, $\hbar\omega_{pl} > 0.2$ eV) and small dimensions, respectively. Finally, interactions with SO phonons can also influence the lifetimes of hybrid plasmon–phonon modes, especially when the energy of the hybrid mode is close to that of the SO phonons[38]. Our scaled graphene nanoribbons with different widths enable us to identify the damping mechanisms of graphene plasmons in a comprehensive manner.

From the extinction spectra in Figs 2a and 3a, the plasmon damping rate $\Gamma_p$ can be extracted from the resonance linewidth using a simple procedure as described in Supplementary Section SII. Figure 4a plots the extracted $\Gamma_p$ as a function of the effective ribbon width $W_e$. For the hybrid plasmon–phonon modes on $SiO_2$, only peak 3 is plotted because it exists for all of the differently sized ribbons. On a DLC substrate, because the plasmon resonance energy is always below the optical phonon energy, the dominant broadening mechanism involves elastic carrier scattering processes. Indeed, its damping rate increases as $W_e$ decreases, indicative of scattering at the edges of the ribbon. A similar damping effect for plasmons in metallic nanoparticles has been extensively studied[13,14]. This effect can be modelled using[13,14] $\Gamma_p = \Gamma_0 + a/W_e$, where $\Gamma_0$ is the damping rate due to carrier scattering in bulk graphene, which was measured to be $\sim$69 cm$^{-1}$ from the Drude response[18] of large-area, unpatterned graphene nearby on the same DLC substrate, and $a$ is a fitting parameter. This approach was also used to describe damping in metal nanoparticles. We also

want to emphasize that in microscale plasmonics structures, the damping rate $\Gamma_0$ is almost identical to that extracted from the Drude response, indicating the weak impact of the edges. In the fit, $a \approx 2 \times 10^6$ m s$^{-1}$, of the order of the Fermi velocity, as expected from the edge scattering point of view. The DLC data therefore provide us with a good measure of damping due to edge scattering, which will prove useful in our analysis of additional damping channels for graphene ribbons on $SiO_2$ substrates.

Despite the similar characteristics of nanoribbons themselves (that is, similar $\Gamma_0$ and doping), the plasmon damping of ribbons on $SiO_2$ is very different, as shown in Fig. 4a, when compared with ribbons on DLC. First, we emphasize that the damping of hybrid plasmon–phonon modes depends on the relative plasmon versus phonon character. For example, the mode described by peak 3 in Fig. 3a is predominantly phonon-like for large $W_e$, as it resonates near the SO phonon frequency $\omega_{sp2}$. As a result, its damping is determined primarily by the SO phonon lifetime (Supplementary Section SII), which is typically in the picosecond regime. This explains the lower damping rate of this mode compared to the ribbons on DLC in the large $W_e$ limit, as shown in Fig. 4a for $W_e > 120$ nm. Similarly, the small linewidths for peaks 1 and 2 in Fig. 3a can also be accounted for using the same reasoning. On the other hand, in narrower ribbons (that is, $W_e < 90$ nm), the mode described by peak 3 disperses rapidly in frequency and becomes plasmon-like. However, in contrast to the DLC case, where the plasmon frequency is lower for ribbons of the same width as a result of the different dielectric environments, it has a plasmon frequency larger than the graphene optical phonon frequency of 1,580 cm$^{-1}$. In this case, the plasmon can decay into electron–hole pairs via the emission of a graphene optical phonon, thereby explaining the larger damping. This process is schematically illustrated in Fig. 4b, and the following quantitative modelling verifies this mechanism.

Figure 4c plots the plasmon lifetime as a function of plasmon frequency instead of damping rate. The plasmon lifetime in graphene ribbons on DLC can be modelled by $\tau = [\Gamma_0 + a/W_e + \Gamma_{ep}]^{-1}$, where $\Gamma_{ep}$ is the additional damping due to optical phonon excitations. $\Gamma_{ep}$ can be calculated from the electron self-energy due to interaction with the optical phonon[42,44], although its effect is relatively small for our measured ribbons on DLC. Lifetime modelling of the hybrid plasmon–phonon mode (that is, peak 3) in the $SiO_2$ counterpart is more involved (Supplementary Section SII). After accounting for the plasmon decay channel via optical phonons, good agreement is achieved for plasmon lifetimes on both DLC and $SiO_2$, as shown in Fig. 4c. In $SiO_2$, the hybrid mode begins with a long lifetime in the vicinity of the SO phonon energy at 1,168 cm$^{-1}$, but deteriorates rapidly to 20 fs as its plasmon energy exceeds the optical phonon energy. The plasmon lifetime of 20 fs corresponds to a propagation length of 200 nm due to energy dissipation at a frequency of ~2,000 cm$^{-1}$ (plasmon mode area $\sim 2 \times 10^{-3}$ μm$^2$). This observation clearly highlights the important role of the various phonons regarding plasmon lifetime. Moreover, Fig. 4c shows that for the same frequency plasmon mode, the lifetime of plasmon on DLC is much shorter than that on $SiO_2$. This is due to the fact that to have the same plasmon frequencies, ribbons on DLC have to be much narrower than those on $SiO_2$, and edge scattering is more pronounced.

We strengthen our case for plasmon decay via optical phonons by studying the carrier density dependence of the plasmon linewidth. Figure 4d shows the extinction spectra of a ribbon array with a width of 100 nm on $SiO_2$, at four different doping concentrations. Procedures for adjusting the doping are described in the Methods. We observed an increase in plasmon resonance frequency and amplitude with doping, as expected from the carrier density scaling law in graphene[4]. As the plasmon frequency exceeds the graphene optical phonon energy, we observed a substantial increase in its resonance linewidth, as demonstrated in the inset of Fig. 4d. In contrast, the plasmon resonance linewidth decreases slightly with doping in the far-infrared regime for graphene microstructures[8]. This observation further reinforces our picture of the plasmon decay channel via optical phonon emission.

## Outlook for graphene plasmonics

By the scaling of plasmonic structures into the nanometre regime we can unravel the importance of both substrate and intrinsic optical phonons for plasmon dispersion and lifetimes. These new findings have important implications for furthering our understanding of basic electronic properties such as carrier screening, scattering and energy dissipation[23,24,39,40,45,46]. Most importantly, our study provides important guidelines for the design of future graphene-based plasmonic devices. Indeed, interaction with optical phonons in graphene limits the quality factor of the plasmon resonance beyond the optical phonon frequency. As a result, the optimal operation wavelength of future graphene plasmonic devices should lie between the subterahertz regime and 6.5 μm. Nevertheless, the hybridized plasmon–phonon mode in the vicinity of the surface polar phonon frequency features a long lifetime. It might be promising to exploit this for high-performance mid-infrared photonic devices.

## Methods

Large-scale graphene was grown using CVD on copper foil and was then transferred to $SiO_2$/silicon or DLC/silicon substrates[15], before subsequent electron-beam lithography and oxygen plasma etching. The fabricated nanoribbon arrays were designed to have widths $W$ equal to the spacing between adjacent ribbons, thereby corresponding to a filling factor of 50%. The array size was 70 μm × 70 μm, significantly larger than the infrared beam size (diameter, ~25 μm) used in the experiments. The as-prepared samples were hole-doped with a Fermi level of approximately −0.3 eV. By exposing the samples to nitric acid vapour for 10 min, the Fermi level could be decreased further to below −0.5 eV. Baking the doped sample at 170 °C could reduce the doping significantly. As a result, by adjusting the doping and baking times, we can achieve various doping concentrations, which can be determined using the extinction spectra in the far-infrared[18]. In the transmission measurements, we first recorded the transmission spectrum $T_{per}$ for light perpendicularly polarized with respect to the ribbons, and the extinction spectra for this particular polarization ($1 - T_{per}/T_0$) were obtained using the transmission of the bare substrate (with oxide but no graphene ribbons), $T_0$, as reference. The extinction spectrum ($1 - T_{par}/T_0$) for light with polarization parallel to the nanoribbons was obtained in a similar manner. Light transmission through the substrate without graphene $T_0$ has no polarization dependence. As shown in Fig. 1c, the extinction spectrum for parallel light polarization ($1 - T_{par}/T_0$) was close to zero over the entire wavelength of interest. Consequently, for simplicity we used $1 - T_{per}/T_{par}$ for the extinction spectrum of the light with perpendicular polarization, because in this case no reference point is necessary.

Received 22 October 2012; accepted 13 February 2013; published online 14 April 2013

## References


1. Maier, S. *Plasmonics: Fundamentals and Applications* 1st edn (Springer, 2007).
2. Koppens, F. H. L., Chang, D. E. & Garcia de Abajo, F. J. Graphene plasmonics: a platform for strong light–matter interactions. *Nano Lett.* **11,** 3370–3377 (2011).
3. Vakil, A. & Engheta, N. Transformation optics using graphene. *Science* **332,** 1291–1294 (2011).
4. Ju, L. *et al.* Graphene plasmonics for tunable terahertz metamaterials. *Nature Nanotech.* **6,** 630–634 (2011).
5. Fei, Z. *et al.* Infrared nanoscopy of Dirac plasmons at the graphene/$SiO_2$ interface. *Nano Lett.* **11,** 4701–4705 (2011).
6. Fei, Z. *et al.* Gate-tuning of graphene plasmons revealed by infrared nano-imaging. *Nature* **487,** 82–85 (2012).
7. Chen, J. *et al.* Optical nano-imaging of gate-tunable graphene plasmons. *Nature* **487,** 77–81 (2012).
8. Yan, H. *et al.* Tunable infrared plasmonic devices using graphene/insulator stacks. *Nature Nanotech.* **7,** 330–334 (2012).
9. Yan, H. *et al.* Infrared spectroscopy of tunable Dirac terahertz magneto-plasmons in graphene. *Nano Lett.* **12,** 3766–3771 (2012).
10. Han, M. Y., Ozyilmaz, B., Zhang, Y. & Kim, P. Energy band-gap engineering of graphene nanoribbons. *Phys. Rev. Lett.* **98,** 206805 (2007).

11. Berger, C. *et al.* Electronic confinement and coherence in patterned epitaxial graphene. *Science* **312,** 1191–1196 (2006).
12. Todd, K., Chou, H. T., Amasha, S. & Goldhaber-Gordon, D. Quantum dot behavior in graphene nanoconstrictions. *Nano Lett.* **9,** 416–421 (2008).
13. Kreibig, U. & Vollmer, M. *Optical Properties of Metal Clusters* 1st edn (Springer, 1995).
14. Link, S. & El-Sayed, M. A. Size and temperature dependence of the plasmon absorption of colloidal gold nanoparticles. *J. Phys. Chem. B* **103,** 4212–4217 (1999).
15. Li, X. *et al.* Large-area synthesis of high-quality and uniform graphene films on copper foils. *Science* **324,** 1312–1314 (2009).
16. Wu, Y. *et al.* High-frequency, scaled graphene transistors on diamond-like carbon. *Nature* **472,** 74–78 (2011).
17. Kucírková, A. & Navrátil, K. Interpretation of infrared transmittance spectra of $SiO_2$ thin films. *Appl. Spectrosc.* **48,** 113–120 (1994).
18. Yan, H. *et al.* Infrared spectroscopy of wafer-scale graphene. *ACS Nano* **5,** 9854–9860 (2011).
19. Fuchs, R. & Kliewer, K. L. Optical modes of vibration in an ionic crystal slab. *Phys. Rev.* **140,** A2076–A2088 (1965).
20. Dubois, L. H. & Schwartz, G. P. Surface optical phonons and hydrogen chemisorption on polar and nonpolar faces of GaAs, InP, and GaP. *Phys. Rev. B* **26,** 794–802 (1982).
21. Matz, R. & Luth, H. Conduction-band surface plasmons in the electron-energy-loss spectrum of GaAs(110). *Phys. Rev. Lett.* **46,** 500–503 (1981).
22. Wang, S. Q. & Mahan, G. D. Electron scattering from surface excitations. *Phys. Rev. B* **6,** 4517–4524 (1972).
23. Fratini, S. & Guinea, F. Substrate-limited electron dynamics in graphene. *Phys. Rev. B* **77,** 195415 (2008).
24. Hwang, E. H., Sensarma, R. & Das Sarma, S. Plasmon–phonon coupling in graphene. *Phys. Rev. B* **82,** 195406 (2010).
25. Liu, Y. & Willis, R. F. Plasmon–phonon strongly coupled mode in epitaxial graphene. *Phys. Rev. B* **81,** 081406 (2010).
26. Stern, F. Polarizability of a two-dimensional electron gas. *Phys. Rev. Lett.* **18,** 546–548 (1967).
27. Wunsch, B., Stauber, T. & Guinea, F. Dynamical polarization of graphene at finite doping. *New J. Phys.* **8,** 318 (2006).
28. Hwang, E. H. & Das Sarma, S. Dielectric function, screening, and plasmons in two-dimensional graphene. *Phys. Rev. B* **75,** 205418 (2007).
29. Mikhailov, S. A. & Savostianova, N. A. Microwave response of a two-dimensional electron stripe. *Phys. Rev. B* **71,** 035320 (2005).
30. Nikitin, A. Yu , Guinea, F., Garcia-Vidal, F. J. & Martin-Moreno, L. Surface plasmon enhanced absorption and suppressed transmission in periodic arrays of graphene ribbons. *Phys. Rev. B* **85,** 081405 (2012).
31. Thongrattanasiri, S., Manjavacas, A. & Garcia de Abajo, F. J. Quantum finite-size effects in graphene plasmons. *ACS Nano* **6,** 1766–1775 (2012).
32. Radovic, L. R. & Bockrath, B. On the chemical nature of graphene edges: origin of stability and potential for magnetism in carbon materials. *J. Am. Chem. Soc.* **127,** 5917–5927 (2005).
33. Areshkin, D. A., Gunlycke, D. & White, C. T. Ballistic transport in graphene nanostrips in the presence of disorder: importance of edge effects. *Nano Lett.* **7,** 204–210 (2006).
34. Fano, U. Effects of configuration interaction on intensities and phase shifts. *Phys. Rev.* **124,** 1866–1878 (1961).
35. Jablan, M., Soljacic, M. & Buljan, H. Unconventional plasmon–phonon coupling in graphene. *Phys. Rev. B* **83,** 161409 (2011).
36. Mahan, G. D. *Many-Particle Physics* 3rd edn (Kluwer Academic/Plenum, 2000).
37. Ferrari, A. C. *et al.* Raman spectrum of graphene and graphene layers. *Phys. Rev. Lett.* **97,** 187401 (2006).
38. Hillenbrand, R., Taubner, T. & Keilmann, F. Phonon-enhanced light–matter interaction at the nanometre scale. *Nature* **418,** 159–162 (2002).
39. Perebeinos, V. & Avouris, Ph. Inelastic scattering and current saturation in graphene. *Phys. Rev. B* **81,** 195442 (2010).
40. Fischetti, M. V., Neumayer, D. A. & Cartier, E. A. Effective electron mobility in Si inversion layers in metal–oxide–semiconductor systems with a high-κ insulator: the role of remote phonon scattering. *J. Appl. Phys.* **90,** 4587–4608 (2001).
41. Adato, R. *et al.* Radiative engineering of plasmon lifetimes in embedded nanoantenna arrays. *Opt. Express* **18,** 4526–4537 (2010).
42. Jablan, M., Buljan, H. & Soljacic, M. Plasmonics in graphene at infrared frequencies. *Phys. Rev. B* **80,** 245435 (2009).
43. Langer, T. *et al.* Plasmon damping below the Landau regime: the role of defects in epitaxial graphene. *New J. Phys.* **12,** 033017 (2010).
44. Park, C-H., Giustino, F., Cohen, M. L. & Louie, S. G. Velocity renormalization and carrier lifetime in graphene from the electron–phonon interaction. *Phys. Rev. Lett.* **99,** 086804 (2007).
45. Low, T. *et al.* Cooling of photoexcited carriers in graphene by internal and substrate phonons. *Phys. Rev. B* **86,** 045413 (2012).
46. Ong, Z. & Fischetti, M. V. Theory of interfacial plasmon–phonon scattering in supported graphene. *Phys. Rev. B* **86,** 165422 (2012).


## Acknowledgements

The authors thank B. Ek, J. Bucchignano and S. (Jay) Chey for technical assistance, and V. Perebeinos and Z. Li of the National High Magnetic Field Laboratory and T.F. Heinz of Columbia University for discussions. F.X. thanks C. Gmachl of Princeton University and Y. Yao of Harvard University for help in the planning stage of the project. T.L. and F.G. acknowledge the hospitality of KITP, supported in part by the National Science Foundation (grant no. NSF PHY11-25915). T.L. also acknowledges partial support from NRI-INDEX, and F.G. is also supported by the Spanish MICINN (FIS2008-00124, CONSOLIDER CSD2007-00010) and ERC grant 290846.

## Author contributions

F.X. and H.Y. initiated the project and conceived the experiments. W.Z., Y.W., H.Y. and F.X. fabricated the devices. H.Y. performed the measurements and data analysis. T.L. and F.G. provided modelling and the theoretical foundation. M.F. participated in setting up the experimental apparatus. X.L. grew the CVD graphene. H.Y. and T.L. co-wrote the manuscript with input from F.X., and P.A. provided suggestions throughout the project. All authors commented on the manuscript.

## Additional information

Supplementary information is available in the online version of the paper. Reprints and permissions information is available online at www.nature.com/reprints. Correspondence and requests for materials should be addressed to H.Y., P.A. and F.X.

## Competing financial interests

The authors declare no competing financial interests.